pH-Activatable Cyanine Dyes for Selective Tumor Imaging Using Near-infrared Fluorescence and Photoacoustic Modalities

Huiying Mu,[1] Koji Miki,[1]* Hiroshi Harada,[2] Kouki Tanaka,[1] Kohei Nogita,[1] and Kouichi Ohe[1]*

[1]Department of Energy and Hydrocarbon Chemistry, Graduate School of Engineering, Kyoto University, Katsura, Nishikyo-ku, Kyoto 615-8510, Japan.

[2]Laboratory of Cancer Cell Biology, Radiation Biology Center, Kyoto University, Yoshida, Sakyo-ku, Kyoto 606-8501, Japan.

KEYWORDS: photoacoustic imaging, fluorescence, pH-activatable, tumor-targeting, cyanine dyes

ABSTRACT: Photoacoustic (PA) imaging is an emerging molecular imaging modality that complements fluorescence imaging and enables high resolution within deep tissue. Fluorescence/PA multimodality imaging would be a powerful technique to extract more comprehensive information from targets than traditional single-modality imaging. In this paper, we developed a new pH-activatable sensor, **CypHRGD**, which is applicable to both fluorescence and PA detection. **CypHRGD** was derived from our previous near-infrared pH-sensing platform, in which substitution with a bulky phenyl group and functionalization with a cRGD peptide remarkably improved the sensor's biocompatibility with attenuated dye aggregation. The multimodality imaging applications of **CypHRGD** were demonstrated in cultured cells and cancer-xenografted mice with rapid kinetics, high sensitivity and specificity, which relies on cRGD-facilitated tumor targeting and probe accumulation and subsequent activation in the acidic organelles after endocytosis.

Molecular imaging has been proposed to aid cancer surgery by providing selective imaging of tumors, especially tiny ones (<2-3 mm), over the normal tissues and

identifying the border between them.[1-4] Fluorescence imaging is a widely adopted imaging modality because of low cost, easy operation, high sensitivity, and high temporal resolution.[5-8] However, one critical limitation of fluorescence imaging is the shallow imaging depth (~1 mm) when applied in vivo. In this regard, photoacoustic (PA) imaging offers a promising complementary method.[9-12] Because of the significantly decreased scattering of the sound relative to light in tissues, PA imaging enables high-resolution imaging at centimeter depths.[13-16] Therefore, fluorescence/PA multimodality imaging would provide a powerful method to obtain deeply penetrated imaging of tumors in vivo with high specificity.[17-23]

Near-infrared (NIR) fluorophores with high extinction coefficients are ideal for both fluorescence and PA imaging in vivo.[24,25] Indocyanine green (ICG, ~1.0×10^5 M^{-1} cm^{-1} at 780 nm) is an excellent candidate, and it has been used as an approved contrast agent for medical imaging.[26,27] For specific and sensitive tumor imaging, the ICG dye must be functionalized as an activatable sensor to achieve a high tumor-to-background ratio.[28-29] Alteration in the NIR absorption of ICG should be an effective way to modulate the fluorescence and PA signals simultaneously. We have previously reported a new ICG-based pH-sensing platform where a nucleophilic mercapto group was introduced to the side chain of one benzoindole nitrogen (Figure 1a).[30] The dye can form a cyclic structure **CypH1-C** under basic conditions, which blocks the π-conjugation of ICG for the NIR absorption and exhibits a nonemissive property. Upon protonation of the sulfur moiety under acidic conditions, the ring-opening process occurs to form **CypH1-O** and the NIR absorption and emission are recovered. Here we report the use of our ICG-derived pH sensors for selective tumor visualization by both fluorescence and PA imaging, ranging from cultured cells to living animals. To date, a few pH sensors available for the fluorescence/PA dual imaging have been reported.[31,32] However, they require relatively long time for specific tumor imaging (10 h to days). To facilitate the tumor recognition, in this work, we incorporated a tumor-targeting short peptide c(RGDfK) (cRGD)[33] and indeed observed earlier tumor imaging (at 6 h after injection) than the control molecule without cRGD.

In this study, we selected the mercapto-substituted pH sensor **CypH1** for tumor imaging because of its appropriate pK_a (4.9), which allows high-contrast imaging of acidic

intracellular compartments. Compared with the dispersed state with surfactant Triton X-100, **CypH1** undergoes facile aggregation in aqueous solution because of its poor water solubility, which may hamper its use in biological systems (Figure S2a). To address this issue, we first prepared **CypH2** by introducing a water-soluble sulfonate group to the side chain of **CypH1** (Figure 1b). However, the absorption spectrum of **CypH2** in 0.1 M PBS still showed an absorption peak at 800–850 nm attributed to monomers and a blue-shifted shoulder peak at 700–750 nm attributed to H-aggregates (Figure S2b).[34,35] The ratio of aggregated and nonaggregated dyes were calculated as 0.89 ($A_{745\ nm}$/ $A_{810\ nm}$). We next replaced one methyl group in the benzoindole moiety with a relatively bulky phenyl group to suppress the dye aggregation (Figure S2c). Indeed, **CypH3** reduced dye aggregation with low aggregated ratio ($A_{745\ nm}$/ $A_{810\ nm}$ = 0.69). To obtain information about the structure of the cyanine dyes, we performed density functional theory (DFT) calculations at the B3LYP/6-31G* level (Figure S3). The optimized structure of **CypH3-O** showed that the phenyl substituent was vertical to the π-conjugated plane. This may contribute to the attenuated intermolecular dye stacking. Finally, we introduced the cRGD peptide to the phenyl group, and the dye aggregation of **CypHRGD** was further reduced (($A_{745\ nm}$/ $A_{810\ nm}$ = 0.60), which is comparable to that in the highly dispersed state with surfactant (Figure S2d). More importantly, the cRGD peptide served as a tumor-targeting moiety, which can specifically and strongly bind $\alpha_v\beta_3$ integrin receptor (ABIR).[36,37] We also expected that the receptor-mediated endocytosis upon cRGD-ABIR recognition may facilitate the activation of pH sensors inside the acidic organelles, and the relatively small size of cRGD can provide rapid clearance of small-molecule dyes.

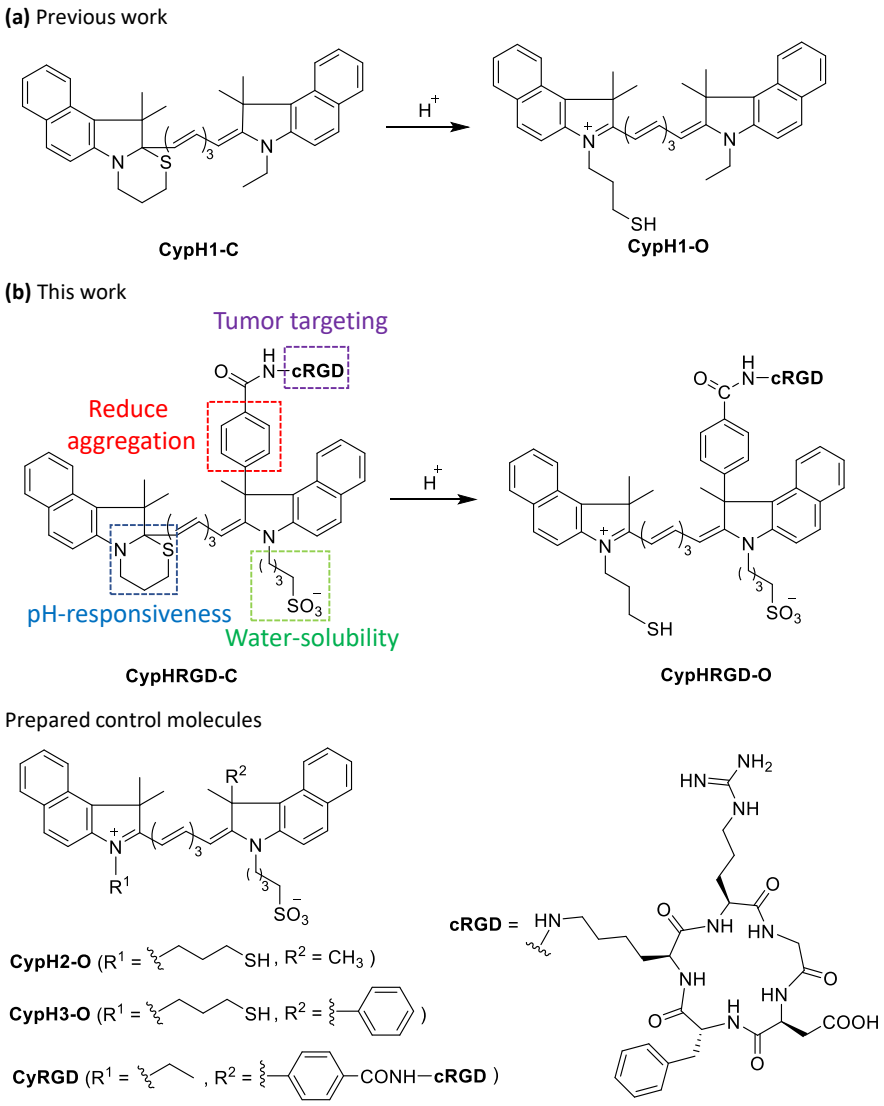

Figure 1. pH-responsive ICG derivatives (a) **CypH1** and (b) **CypHRGD**. Insert: chemical structures of the prepared control molecules **CypH2**, **CypH3**, and **CyRGD**. Equilibrium between **CypH1-C** or **CypHRGD-C** having an open-ring structure and **CypH1-O** or **CypHRGD-O** having a closed-ring structure.

We next examined the spectroscopic properties of **CypHRGD** for pH sensing. Similar to the parent sensor **CypH1**, **CypHRGD** dominated the closed-ring form under basic and neutral conditions and showed very weak absorption and emission in the NIR region. As the pH of the solution decreased, the closed-ring structure was gradually transformed to

the corresponding open-ring form, accompanied by increased NIR absorption and emission centered at 800 nm and 825 nm, respectively (Figure 2a, 2b). The pH titration experiments showed a pH-sensitive range located between 4 and 6 (Figure 2c), which matches the pH of acidic cellular organelles. The largely pH-dependent alteration in the NIR absorption confers the potential for **CypHRGD** to act as a pH-activatable PA sensor. We, therefore, measured its PA signals upon irradiation with a pulsed laser at 780 nm in a range of pH (Figure 2d). **CypHRGD** indeed showed a pH-dependent PA responsiveness between pH 7.2 and 4.2 with a 5.7-fold change of $PA_{pH4.2}/PA_{pH7.2}$. In contrast, ICG as the control PA dye retained an almost constant PA signal regardless of the pH alteration. Tumor imaging by **CypHRGD** also relies on dye accumulation directed by cRGD. We, therefore, assessed the concentration-dependent absorption, fluorescence, and PA intensity of **CypHRGD**, which showed a linear enhancement as the concentration increased (Figure S4).

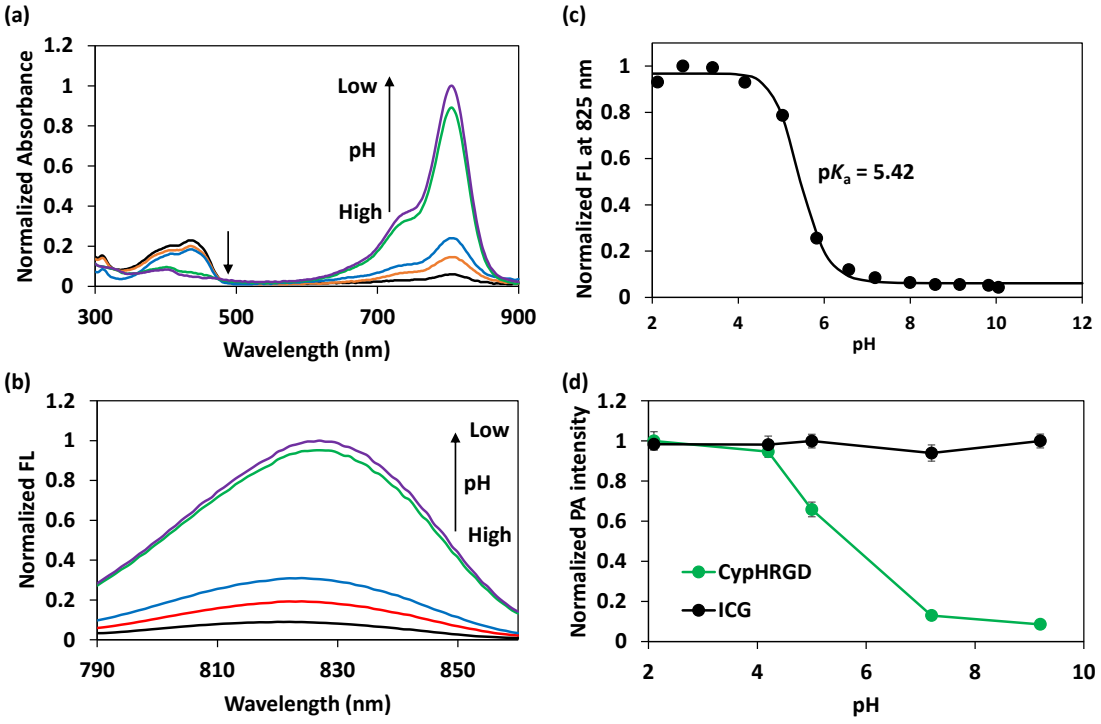

Figure 2. pH-dependent (a) absorption and (b) fluorescence spectral changes of **CypHRGD** (5 μM) in buffered aqueous solution with different pH values (pH= 9.2, 7.2, 5.8, 4.2, 2.1) with Triton X-100 (2.0×10^{-3} M). (c) Fluorescence intensity of **CypHRGD**

in buffered solution normalized at 825 nm. λ_{ex} = 780 nm. The fluorescence intensities were fitted to sigmoid curves (R^2 = 0.997) to determine pK_a values. (d) Normalized photoacoustic (PA) intensity of dye ICG and **CypHRGD** (20 μM) in buffered solutions with different pH values. Error bar indicates standard deviation (s.d.), n = 3.

Encouraged by the favorable pH responsiveness of **CypHRGD**, we next turned our attention to live-cell assays. A549 was selected as a cell line model because it overexpresses ABIR.[37,38] The cytotoxicity of **CypHRGD** was first assessed via MTT assays. A negligible reduction in the cell viability was observed after incubation of **CypHRGD** (up to 10 μM) with A549 cells for 12 h (Figure S10, S11). The fluorescence imaging was performed using an IVIS Spectrum Instrument equipped with an ICG filter (Figure 3a, 3b). The cells were incubated with **CypHRGD** in the serum-free culture medium at 4 °C (on ice, to prevent endocytosis)[30,39,40] or 37 °C for 4 h. Remarkably increased fluorescence was observed in the dishes incubated at 37 °C ($F_{4\ h}/F_{0\ h}$ = 11) but not at 4 ^{o}C, suggesting that **CypHRGD** would be internalized into the cells through ATP-dependent endocytosis and activated in the acidic cellular compartments, such as endosomes and lysosomes (Figure S12). We noticed that the fluorescence of the dishes at 4 °C was almost identical to that of negative control dishes without cells, which indicates the extremely low background signal of **CypHRGD** (Figure S13). To investigate whether the cell internalization of **CypHRGD** was selectively mediated by the cRGD–ABIR recognition, we carried out control imaging experiments at 37 °C: (1) in the presence of competitive cRGD (100 μM, 10 eq.) in A549 cells (Figure 3a, 3b) and (2) in a normal cell line, NIH-3T3 cells (Figure S14), which expresses a low level of ABIR.[41] In both cases, substantially decreased fluorescence was observed compared with that by **CypHRGD** alone in A549 cells.

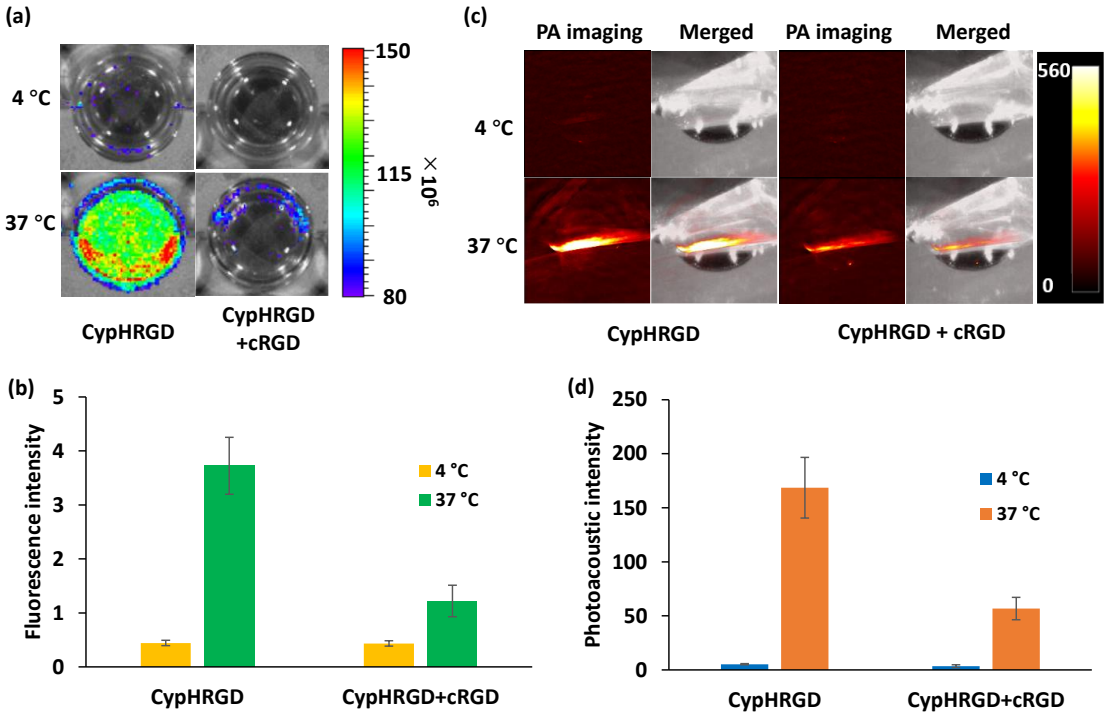

Figure 3. (a) Representative optical images and (b) fluorescence intensity quantification of dishes of A549 cells after incubation for 4 h with **CypHRGD** (10 μM) only or pretreated with free cRGD (10 eq.), then incubated with **CypHRGD** (10 μM) at 4 °C or 37 °C. (c) Representative (PA) images and (d) PA intensity quantification of tubes containing A549 cells collected by cell scrapper from the dishes after incubation for 4 h with **CypHRGD** (10 μM) or co-incubated with cRGD (10 eq.) and **CypHRGD** (10 μM) at 4 °C or 37 °C. Error bar indicates s.d., n = 3.

To determine the subcellular localization of **CypHRGD** after uptake into living cells, we performed confocal imaging (Figure S15). Although the maximum absorbance wavelength of **CypHRGD** is at 810 nm, it could be moderately excited by the 633 nm laser (4.1% relative to the peak value). The intracellular fluorescence was gradually increased as the incubation time increased, which was consistent with the IVIS imaging results. Furthermore, it showed punctate patterns that can be colocalized with LysoTracker, a fluorescent stain for acidic organelles such as lysosomes and endosomes, with a Pearson correlation factor of 0.8. It is worth noting that the extracellular and plasma membrane signals remained minimal during the imaging. These results again verified that

CypHRGD was taken up into living cells through endocytosis, and activated in the intracellular acidic organelles.

To measure the PA signals in living cells, we collected the cells in Eppendorf tubes and subjected them to PA imaging (Figure 3c, 3d). Similar to the fluorescence imaging results, the PA signals were significantly increased after the cells were incubated with **CypHRGD** at 37 °C for 4 h ($F_{4\,h}/F_{0\,h}$ = 16), which could be attenuated in the presence of excess cRGD. However, the dishes without cells or incubated at 4 °C showed much weaker PA signals. In contrast, the ICG dye always showed bright fluorescence and PA signals despite incubation time and temperature (Figure S16).

We finally attempted to apply **CypHRGD** to *in vivo* tumor imaging. A549 cells were xenografted, and the tumors were developed into the right legs of nude living mice. **CypHRGD** was intravenously (*i.v.*) administrated into the tumor-bearing mice, and the IVIS fluorescence images were recorded at different time points (Figure 4a). The accumulation and activation of **CypHRGD** at the tumor was certified as early as 6 h after the injection and reached a maximum after 9 h (Figure 4c). Twenty-four hours after administration, the mice were sacrificed and dissected for *ex vivo* imaging of the organs (Figure 4b). It showed that fluorescence in the tumor was much brighter than that in other organs, including lung, heart, kidney, and spleen (Figure 4d). Not surprisingly, the sensors also accumulated in the liver sites, probably because the liver is primarily responsible for the excretion of sensor molecules. Under identical conditions, we also assessed two control molecules, **CypH3** and **CyRGD**, for tumor imaging in mice, which lack cRGD and the pH-sensitive moiety, respectively. Distinct tumor imaging could also be observed using **CypH3**, but it showed much-delayed kinetics, reduced intensity, and moderate selectivity when compared with **CypHRGD**. This highlighted the importance of the cRGD moiety in **CypHRGD**, which facilitates specific dye accumulation in the tumor expressing integrins and the subsequent activation in acidic organelles following the receptor-mediated endocytosis. As for the pH-insensitive probe, **CyRGD** represents the conventional “always-on” imaging probe that requires a relatively long time to be cleared from normal tissues for high-contrast tumor imaging. Indeed, **CyRGD** emitted bright but indiscriminate fluorescence throughout the body of the mice until 24 h post-injection, which showed a moderate tumor selectivity in the low-contrast image (Figure S17). We

further applied **CypHRGD** to in vivo PA imaging in tumor-bearing living nude mice by *i.v.* injection, and the PA signals of the tumor sites were measured at the indicated post-injection time points (Figure 5). After subtracting the background signals from hemoglobin proteins, a significant time-dependent increase in the PA signal of the tumor was observed as early as 3 h after the injection. These results successfully demonstrated the utility of **CypHRGD** for selective and rapid tumor imaging in living mice using both NIR fluorescence and PA imaging with high contrast.

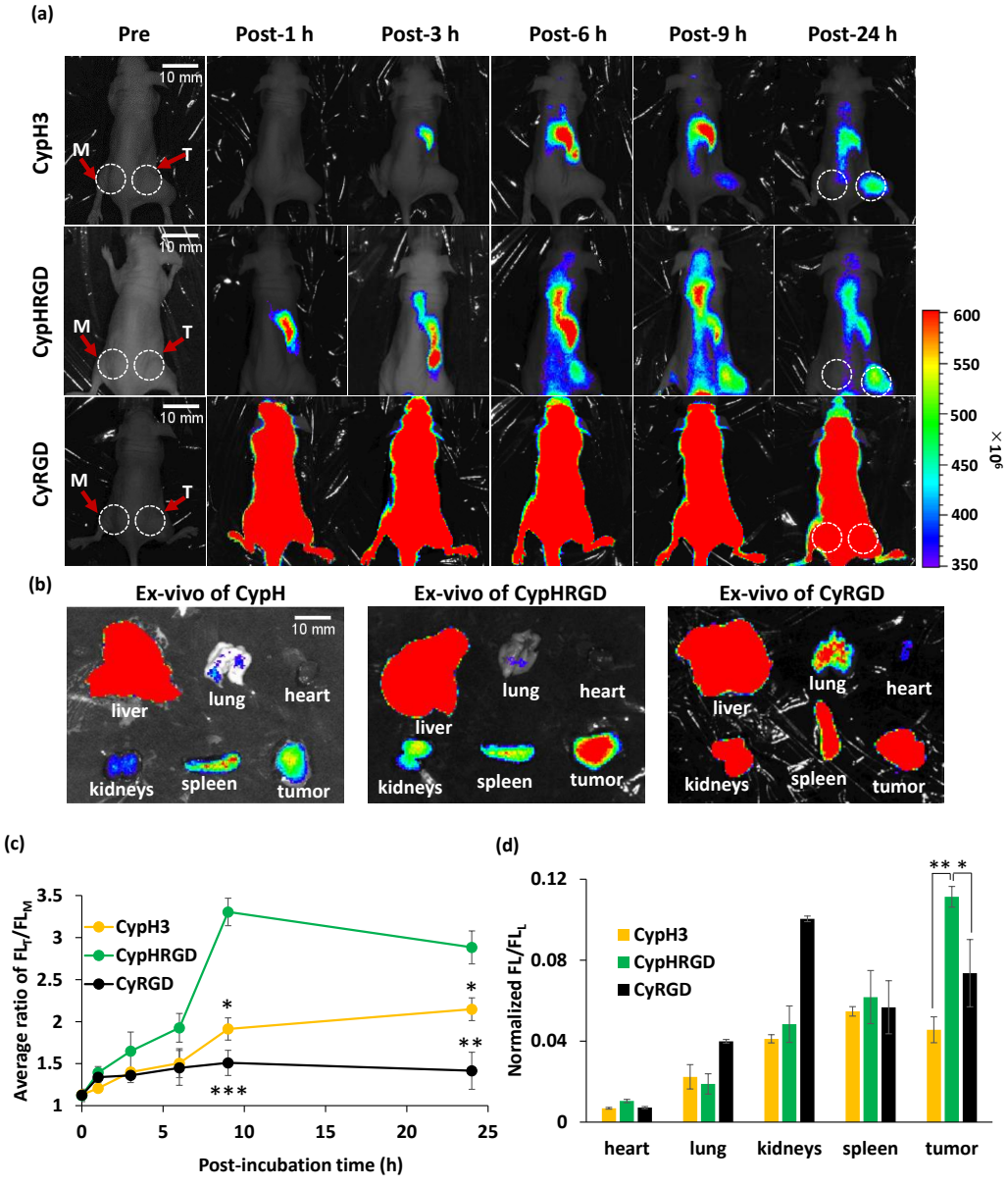

Figure 4. *In vivo* and *ex vivo* NIRF imaging of tumor-bearing mice by using probe **CypHRGD** and control molecules **CypH3** and **CyRGD**. (a) Real-time fluorescence imaging of tumor-bearing mouse after administration of **CypH3**, **CypHRGD**, and **CyRGD** (100 μM in 200 μL saline) at different time point. White circles indicate the position of muscle and tumor tissue. T: tumor; M: muscle. (b) *Ex vivo* images of individual organs and tumors at 24 h post-injection. (c) Normalized fluorescence intensity ratio of tumor area (FL_T) to muscle area (FL_M) as a function of post-injection time for the mice in (a). (d) The quantification of fluorescence ratio (FL/FL_L) of fluorescence intensity in organs or tumor to that in liver in (b). L: liver. Scale bar: 10 mm. Statistical analyses were performed with a two-tailed Student's *t*-test (n = 3) relative to the data of **CypHRGD**-treated mice. *: $P < 0.1$, **: $P < 0.05$, ***: $P < 0.001$. Error bar indicates s.d. of independent experiments (n = 3).

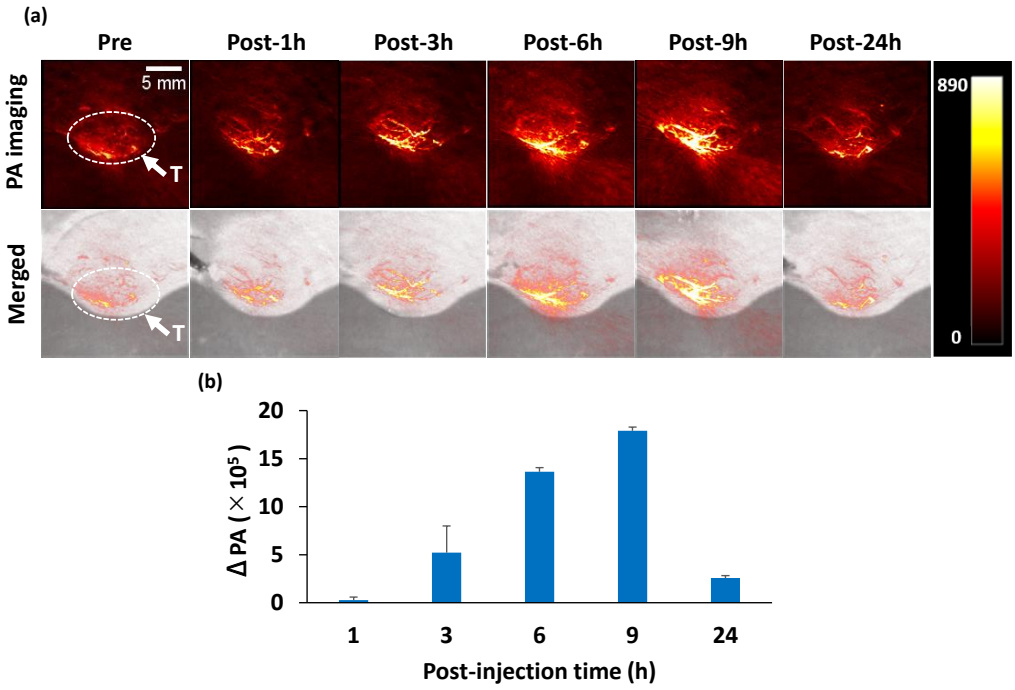

Figure 5. PA images of living nude mice bearing tumor (A549 cells). (a) Representative PA images of the tumor-bearing mice were obtained before injection or 1, 3, 6, 9, and 24 h after injection of **CypHRGD** (100 μM in 200 μL saline). White circles indicate the

position of tumor sites. T: tumor. (b) Enhancement of PA signals of tumor sites ($PA–PA_{pre}$) as a function of post-injection time. Scale bar: 5 mm. Error bar indicates s.d., n = 3.

In summary, we have synthesized a new pH-activatable NIR sensor, **CypHRGD**, based on our ICG-derived pH-sensing platform. **CypHRGD**, consisting of a sulfonate group, bulky phenyl substituent and the cRGD peptide, greatly attenuated the dye aggregation. The pH-modulated ring-opening/closing process resulted in a significant change in the NIR absorption, allowing for robust pH responsiveness between pH 4 and 6 by both fluorescence and PA detection. Furthermore, we demonstrated the utility of **CypHRGD** for both fluorescence and PA imaging in cultured cancer cells and cancer-xenografted living mice. Rapid, selective, and sensitive tumor imaging was attained owing to the cRGD-mediated tumor recognition and probe accumulation, as well as the pH-dependent activation in acidic organelles after endocytosis. The optimization of imaging sensitivity and specificity by encapsulating/grafting the NIR pH-activatable sensors into/on biocompatible and tumor-targeting nanomaterials is under way in our group.

ASSOCIATED CONTENT

Supporting Information.

This material is available free of charge via the Internet at http://pubs.acs.org." Synthetic and experimental details, supplementary figures, and scanned spectral data.

AUTHOR INFORMATION

Corresponding Author

Koji Miki—Department of Energy and Hydrocarbon Chemistry, Graduate School of Engineering, Kyoto University, Katsura, Nishikyo-ku, Kyoto 615-8510, Japan; E-mail: kojimiki@scl.kyoto-u.ac.jp. Phone: +81 75 3832497.

Kouichi Ohe—Department of Energy and Hydrocarbon Chemistry, Graduate School of Engineering, Kyoto University, Katsura, Nishikyo-ku, Kyoto 615-8510, Japan; E-mail: ohe@scl.kyoto-u.ac.jp. Phone: +81 75 3832495.

Present Addresses

Huiying Mu—Department of Energy and Hydrocarbon Chemistry, Gradu-ate School of Engineering, Kyoto University, Katsura, Nishikyo-ku, Kyoto 615-8510, Japan;
Hiroshi Harada—Laboratory of Cancer Cell Biology, Radiation Biology Center, Kyoto University, Yoshida, Sakyo-ku, Kyoto 606-8501, Japan;
Kouki Tanaka—Department of Energy and Hydrocarbon Chemistry, Gradu-ate School of Engineering, Kyoto University, Katsura, Nishikyo-ku, Kyoto 615-8510, Japan;
Kohei Nogita—Department of Energy and Hydrocarbon Chemistry, Gradu-ate School of Engineering, Kyoto University, Katsura, Nishikyo-ku, Kyoto 615-8510, Japan.

Author Contributions

The manuscript was written through contributions of all authors. All authors have given approval to the final version of the manuscript.

Notes

The authors declare no competing financial interest.

ACKNOWLEDGMENT

This work was supported by a Grant-in-Aid for Scientific Research on Innovative Areas “Middle molecular strategy: Creation of higher bio-functional molecules by integrated synthesis (No. 2707)” (18H04404) and Grant-in-Aid for Scientific Research (B) (20H02811) of MEXT, Japan. H. M. thanks to a financial support from a Grant-in-aid for JSPS Research Fellows (Grant number 20J15123). K. M. appreciates the financial support from The Naito Foundation and The Ogasawara Foundation for the Promotion of Science & Engineering. A part of this study was conducted through the Joint Usage Program of the Radiation Biology Center, Kyoto University. We acknowledge Professor Teruyuki Kondo and associate Professor Yu Kimura in Kyoto University for photoacoustic (PA) imaging.

REFERENCES

(1) Hussain, T.; Nguyen, Q. T., Molecular imaging for cancer diagnosis and surgery. *Adv. Drug Deliv. Rev.* **2014**, *66*, 90–100.

(2) Kamiya, M.; Urano, Y., Rapid and sensitive fluorescent imaging of tiny tumors in vivo and in clinical specimens. *Curr. Opin. Chem. Biol.* **2016**, *33*, 9–15.

(3) Saeed, M.; Xu, Z.; De Geest, B. G.; Xu, H.; Yu, H., Molecular imaging for cancer immunotherapy: seeing is believing. *Bioconjugate Chem.* **2020**, *31*, 404–415.

(4) Cheng, P.; Pu, K., Activatable phototheranostic materials for imaging-guided cancer therapy. *ACS Appl. Mater. Interfaces* **2020**, *12*, 5286–5299.

(5) Zhu, H.; Fan, J.; Du, J.; Peng, X., Fluorescent probes for sensing and imaging within specific cellular organelles. *Acc. Chem. Res.* **2016**, *49*, 2115–2126.

(6) Specht, E. A.; Braselmann, E.; Palmer, A. E., A critical and comparative review of fluorescent tools for live-cell imaging. *Annu. Rev. Physiol.* **2017**, *79*, 93–117.

(7) Zhu, H.; Hamachi, I., Fluorescence imaging of drug target proteins using chemical probes. *J. Pharm. Anal.* **2020**, *10*, 426–433.

(8) Liu, S.; Xiong, H.; Yang, J.; Yang, S.; Li, Y.; Yang, W.; Yang, G., Discovery of butyrylcholinesterase-activated near-infrared fluorogenic probe for live-cell and in vivo imaging. *ACS Sens.* **2018**, *3*, 2118–2128.

(9) Reinhardt, C. J.; Chan, J., Development of photoacoustic probes for in vivo molecular imaging. *Biochemistry* **2018**, *57*, 194–199.

(10) Knox, H. J.; Chan, J., Acoustogenic probes: a new frontier in photoacoustic imaging. *Acc. Chem. Res.* **2018**, *51*, 2897–2905.

(11) Joseph, J.; Baumann, K. N.; Kohler, P.; Zuehlsdorff, T. J.; Cole, D. J.; Weber, J.; Bohndiek, S. E.; Hernandez-Ainsa, S., Distance dependent photoacoustics revealed through DNA nanostructures. *Nanoscale* **2017**, *9*, 16193–16199.

(12) Baumann, K. N.; Fux, A. C.; Joseph, J.; Bohndiek, S. E.; Hernadez-Ainsa, S., An active DNA-based nanoprobe for photoacoustic pH imaging. *Chem. Commun.* **2018**, *54*, 10176–10178.

(13) Borg, R. E.; Rochford, J., Molecular photoacoustic contrast agents: design principles & applications. *Photochem. Photobiol.* **2018**, *94*, 1175–1209.

(14) Weber, J.; Beard, P. C.; Bohndiek, S. E., Contrast agents for molecular photoacoustic imaging. *Nat. Methods* **2016**, *13*, 639–650.

(15) Brown, E.; Brunker, J.; Bohndiek, S. E., Photoacoustic imaging as a tool to probe the tumour microenvironment. *Dis. Model Mech.* **2019**, *12*, dmm039636.

(16) Ma, G.; Gao, X.; Jiang, C.; Xing, S.; Wei, C.; Huang, P.; Lin, J., pH-Responsive nanoprobe for in vivo photoacoustic imaging of gastric acid. *Anal. Chem.* **2019**, *91*, 13570–13575.

(17) Rong, G.; Corrie, S. R.; Clark, H. A., In vivo biosensing: progress and perspectives. *ACS Sens.* **2017**, *2*, 327–338.

(18) Meng, X.; Yang, Y.; Zhou, L.; Zhang, L.; Lv, Y.; Li, S.; Wu, Y.; Zheng, M.; Li, W.; Gao, G.; Deng, G.; Jiang, T.; Ni, D.; Gong, P.; Cai, L., Dual-responsive molecular probe for tumor targeted imaging and photodynamic therapy. *Theranostics* **2017**, *7*, 1781–1794.

(19) Jiang, Y.; Pu, K., Molecular Fluorescence and Photoacoustic Imaging in the Second Near-Infrared Optical Window Using Organic Contrast Agents. *Adv. Biosys.* **2018**, *2*, 1700262.

(20) Gao, X.; Ma, G.; Jiang, C.; Zeng, L.; Jiang, S.; Huang, P.; Lin, J., In vivo near-infrared fluorescence and photoacoustic dual-modal imaging of endogenous alkaline phosphatase. *Anal. Chem.* **2019**, *91*, 7112–7117.

(21) Li, Q.; Li, S.; He, S.; Chen, W.; Cheng, P.; Zhang, Y.; Miao, Q.; Pu, K., An activatable polymeric reporter for near-infrared fluorescent and photoacoustic imaging of invasive cancer. *Angew. Chem.* **2020**, *132*, 7084–7089.

(22) Wang, Y.; Weng, J.; Wen, X.; Hu, Y.; Ye, D., Recent advances in stimuli-responsive in situ self-assembly of small molecule probes for in vivo imaging of enzymatic activity. *Biomater. Sci.* **2020**, DOI: 10.1039/d0bm00895h.

(23) Cheng, H.; Li, Y.; Tang, B. Z.; Yoon, J., Assembly strategies of organic-based imaging agents for fluorescence and photoacoustic bioimaging applications. *Chem. Soc. Rev.* **2020**, *49*, 21–31.

(24) Ji, C.; Cheng, W.; Yuan, Q.; Mullen, K.; Yin, M., From dyestuff chemistry to cancer theranostics: The rise of rylenecarboximides. *Acc. Chem. Res.* **2019**, *52*, 2266–2277.

(25) Huang, J.; Pu, K., Activatable molecular probes for second near-infrared fluorescence, chemiluminescence, and photoacoustic imaging. *Angew. Chem. Int. Ed.* **2020**, *59*, 11717–11731.

(26) Shi, C.; Wu, J. B.; Pan, D., Review on near-infrared heptamethine cyanine dyes as theranostic agents for tumor imaging, targeting, and photodynamic therapy. *J. Biomed. Opt.* **2016**, *21*, 050901.

(27) Namikawa, T.; Iwabu, J.; Munekage, M.; Uemura, S.; Maeda, H.; Kitagawa, H.; Nakayama, T.; Inoue, K.; Sato, T.; Kobayashi, M.; Hanazaki, K., Evolution of photodynamic medicine based on fluorescence image-guided diagnosis using indocyanine green and 5-aminolevulinic acid. *Surg. Today* **2020**, *50*, 821–831.

(28) Guo, Z.; Park, S.; Yoon, J.; Shin, I., Recent progress in the development of near-infrared fluorescent probes for bioimaging applications. *Chem. Soc. Rev.* **2014**, *43*, 16–29.

(29) Sun, W.; Guo, S.; Hu, C.; Fan, J.; Peng, X., Recent development of chemosensors based on cyanine platforms. *Chem. Rev.* **2016**, *116*, 7768–7817.

(30) Miki, K.; Kojima, K.; Oride, K.; Harada, H.; Morinibu, A.; Ohe, K., pH-Responsive near-infrared fluorescent cyanine dyes for molecular imaging based on pH sensing. *Chem. Commun.* **2017**, *53*, 7792–7795.

(31) Chen, Q.; Liu, X.; Chen, J.; Zeng, J.; Cheng, Z.; Liu, Z., A self-assembled albumin-based nanoprobe for in vivo ratiometric photoacoustic pH imaging. *Adv. Mater.* **2015**, *27*, 6820–6827.

(32) Meng, X.; Li, W.; Sun, Z.; Zhang, J.; Zhou, L.; Deng, G.; Gong, P.; Cai, L., Tumor-targeted small molecule for dual-modal imaging-guided phototherapy upon near-infrared excitation. *J. Mater. Chem. B* **2017**, *5*, 9405–9411.

(33) Liu, S., Radiolabeled Cyclic RGD Peptide Bioconjugates as radiotracers targeting multiple integrins. *Bioconjugate Chem.* **2015**, *26*, 1413–1438.

(34) Markova, L. I.; Malinovskii, V. L.; Patsenker, L. D.; Haner, R., J- vs. H-type assembly: pentamethine cyanine (Cy5) as a near-IR chiroptical reporter. *Chem. Commun.* **2013**, *49*, 5298–5300.

(35) Ryu, N.; Okazaki, Y.; Pouget, E.; Takafuji, M.; Nagaoka, S.; Ihara, H.; Oda, R., Fluorescence emission originated from the H-aggregated cyanine dye with chiral gemini surfactant assemblies having a narrow absorption band and a remarkably large Stokes shift. *Chem. Commun.* **2017**, *53*, 8870–8873.

(36) Shaw, S. K.; Schreiber, C. L.; Roland, F. M.; Battles, P. M.; Brennan, S. P.; Padanilam, S. J.; Smith, B. D., High expression of integrin $\alpha_v\beta_3$ enables uptake of targeted fluorescent probes into ovarian cancer cells and tumors. *Bioorg. Med. Chem.* **2018**, *26*, 2085–2091.

(37) Merilahti, P.; Tauriainen, S.; Susi, P., Human parechovirus 1 infection occurs via αVβ1 integrin. *PLoS ONE* **2016**, *11*, 4.

(38) Nestic, D.; Uil, T. G.; Ma, J.; Roy, S.; Vellinga, J.; Baker, A. H.; Custers, J.; Majhen, D., $\alpha_V\beta_3$ integrin is required for efficient infection of epithelial cells with human adenovirus type 26. *J. Virol.* **2019**, *93*, e01474–18.

(39) Seward, G. K.; Wei, Q.; Dmochowski, I. J., Peptide-mediated cellular uptake of cryptophane. *Bioconjugate Chem.* **2008**, *19*, 2129–2135.

(40) Cressman, S. C.; Sun, Y.; Maxwell, E. J.; Fang, N.; Chen, D. Y. Y.; Cullis, P. R., Binding and uptake of RGD-containing ligands to cellular $a_v\beta_3$ Integrins. *Int. Pept. Res. Ther.* **2009**, *15*, 49–59.

(41) Pirroznia, N.; Abdi, K.; Beiki, D.; Emami, F.; Arab, S. S.; Sabzevari, O.; Pakdin-Parizi, Z.; Geramifar, P., Radiosynthesis, biological evaluation, and preclinical study of a ^{68}Ga-labeled cyclic RGD peptide as an early diagnostic agent for overexpressed $\alpha_v\beta_3$ integrin receptors in non-small-cell lung cancer. *Contrast Media Mol. Imaging* **2020**, doi.org/10.1155/2020/8421657.